



Universiteit  
Leiden  
The Netherlands

## Photoinduced processes in dye-sensitized photoanodes under the spotlight: a multiscale in silico investigation

Menzel, J.P.

### Citation

Menzel, J. P. (2022, March 3). *Photoinduced processes in dye-sensitized photoanodes under the spotlight: a multiscale in silico investigation*.

Retrieved from <https://hdl.handle.net/1887/3278038>

Version: Publisher's Version

License: [Licence agreement concerning inclusion of doctoral thesis in the Institutional Repository of the University of Leiden](#)

Downloaded from: <https://hdl.handle.net/1887/3278038>

**Note:** To cite this publication please use the final published version (if applicable).

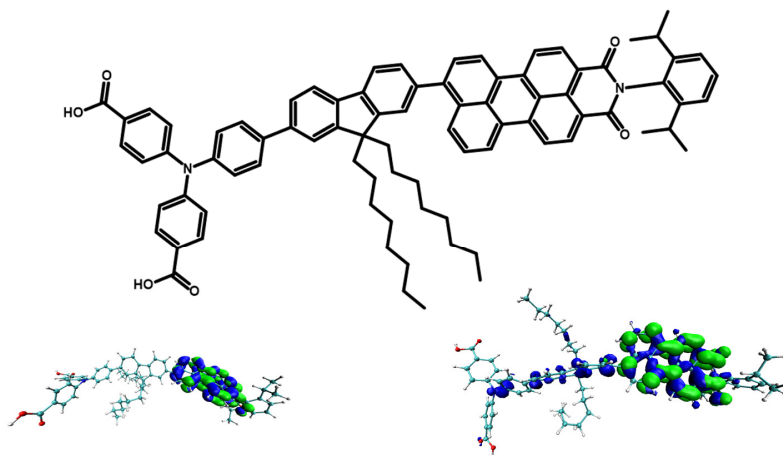


## CHAPTER 6

---

### *In silico* Optimization of Charge Separating Dyes

---



*This Chapter is based in part on:*

Tijmen M.A. Bakker, Jan Paul Menzel, Bas Vreugdenhil, Tessel Bouwens, Simon Mathew, Francesco Buda, Joost N.H. Reek; *to be submitted*

Jan Paul Menzel, Yorrick Boeije, Tijmen M.A. Bakker, Jelena Belić, Huub J.M. de Groot, Lucas Visscher, Joost N.H. Reek, Francesco Buda; *in preparation*



# 6

## **ABSTRACT**

---

While DS-PECs are promising devices in solar energy conversion, a major loss pathway is the charge recombination of electron and hole at the dye-semiconductor interface. Charge separating dyes constructed as push-pull systems can increase the spatial separation of electron and hole, slow down the back-transfer and thereby decrease the recombination rate. In this chapter, we investigate a family of such dyes, consisting of polyphenylamine donors, fluorene bridges and perylene monoimide acceptors using a combination of semi-empirical GFN-xTB ground state dynamics and an AO/MO quantum propagation of photoexcited electron and hole. Several molecular design strategies to increase the charge separation efficiency are investigated *in silico*, including modifying the donor molecule, increasing the bridge length and decoupling the molecular components through steric effects. We find, in agreement with experiment, that exchanging the electron withdrawing formic acid anchors on the triphenylamine donor by electron donating acetic acid ones leads to a more efficient charge separation through hole accumulation on the donor. Triphenylamine donors lead to a more polarized charge transfer state than diphenylamines, while increasing the bridge from one to two fluorene fragments significantly enhances the dye's charge separation capabilities. Decoupling the different components by breaking the conjugation through steric hindrance from side groups results in a better charge separation in comparison to the planar molecule as well. Based on these findings an optimized charge separating dye for efficient suppression of charge recombination is proposed.



## 6.1 Introduction

DS-PECs have shown great promise for the production of renewable fuels, where semiconductor electrodes are sensitized with chromophores that absorb light in the visible range.<sup>1</sup> On the photoanode side, the photoexcited dyes inject the excited electrons into the semiconductor electrode, as discussed in chapter 4, to be used on the photocathode for fuel production. The hole left at the dye can then be picked up by a water oxidation catalyst (WOC) to split water into molecular oxygen and protons, regenerating the ground state of the molecular chromophore.<sup>2</sup>

Water oxidation however is a slow process involving storage of intermediates on long time scales in comparison to the electron injection from the photoexcited dye into the semiconductor anode.<sup>3</sup> Due to the slow consumption of holes by the chemical conversion of water to molecular oxygen and protons, they can be refilled as shown in figure 6.1. Reoccupation of the orbital may occur through a direct recombination of the photoexcited electron in the anode and the hole as seen in red in figure 6.1a, leading to a full deactivation and energetic losses through heat.

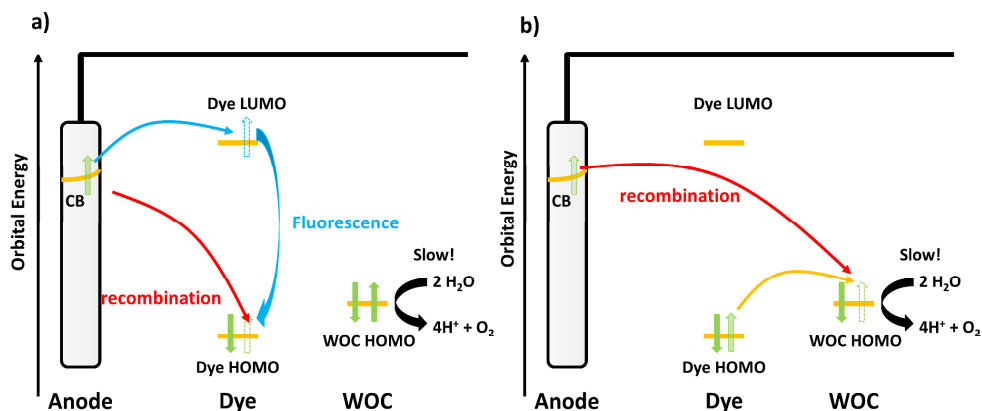


**Figure 6.1.** Energy loss pathways in a dye sensitized photoanode: **a)** After electron injection from the dye into the electrode, the hole on the dye can be either filled by direct recombination (red) with the photoexcited electron or by fluorescence after back transfer of the electron from the semiconductor (blue). **b)** Following the hole transfer to the WOC, recombination of the excited electron from the electrode (red) or back transfer to the dye's HOMO followed by the processes in a) can lead to the loss of the excited state energy.



Another loss pathway shown in blue is through back transfer of the excited electron to the dye followed by fluorescence, where the photoexcited electron falls back to the HOMO while releasing the excess energy in the form of a photon.

Deactivation is also possible after initially successful charge separation and hole transfer to the WOC: the hole at the WOC can be refilled as shown in figure 6.1b. This involves either direct recombination with the photoexcited electron from the semiconductor as shown in red, or back transfer of the hole to the dye as shown in yellow, opening up the loss pathways given in figure 6.1a. All these processes lead to the loss of the photon energy in the form of heat. The factor determining the losses is the ratio between the rates of the competing processes. As the creation of the charge separated state through the electron injection process into  $\text{TiO}_2$  is extremely fast, often in the sub-picosecond or picosecond time frame<sup>4</sup> (see also chapter 4) and the rate of the slowest oxidation step of the WOC ( $^1[\text{Ru(IV)-OH}]^+ \rightarrow ^2[\text{Ru(V)=O}]^+$ ) is, dependent on the concentration of the oxidant, in the order of micro to milliseconds ( $2.3 \times 10^5 \text{ M}^{-1}\text{s}^{-1}$  at 35 °C with  $\text{CeIV}$ ),<sup>5</sup> the time mismatch between these two processes is several orders of magnitude, over which the charge separated state needs to be stabilized. While the last decade has seen important improvements in the turnover frequency of WOCs,<sup>5-9</sup> reducing the charge recombination and back transfer rates is an important factor to minimize losses.

In general, several strategies can be applied to reduce the probability for back-transfer of an electron or hole in a donor-acceptor system. In figure 6.2, some of these possible approaches are schematically shown. When attaching the electron acceptor (such as the dye) directly to the donor, as shown in figure 6.2a, back transfer, though slower than forward charge transfer, can occur relatively unhindered. One way to reduce the rate of back transfer is to introduce a barrier between donor and acceptor by including a molecular system with a HOMO energy higher than that of both donor and acceptor as seen in figure 6.2b.



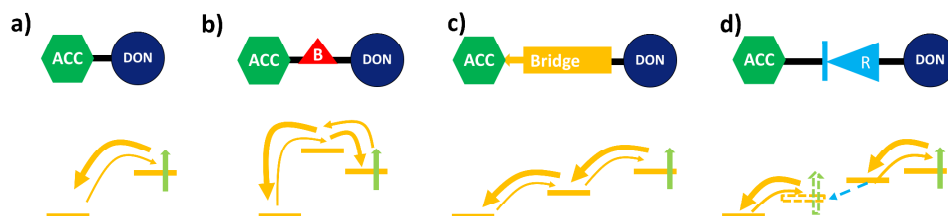


**Figure 6.2.** Schematic representation of different approaches to reduce the back transfer from the acceptor (ACC) towards the donor (DON) after initial charge transfer: **a)** Direct attachment of acceptor and donor allows for relatively easy back transfer. **b)** Introducing an energetic barrier reduces the rate of initial charge transfer, but also reduces the back transfer rate significantly. **c)** Spatial separation via a bridge leads to lower back transfer probability. **d)** Introduction of a molecular rectifier, that through asymmetrical HOMO and LUMO localization or resonant conformational changes increases charge flow in one direction, while decreasing it in the opposite.

While the initial transfer rate is decreased, since this barrier needs to be overtaken, the back transfer rate is even more reduced. Another possible strategy, for example used in natural photosynthesis,<sup>10</sup> is separating electron and hole spatially as quickly as possible by introducing a bridge consisting of one or more electronic systems with clear energy gradients of the involved orbitals as shown in figure 6.2c. Molecules, where HOMO and LUMO are on spatially different components, or molecules that change conformation upon population of the LUMO are efficient ways to allow for charge transfer in one direction but inhibit migration in the opposite direction as shown schematically in figure 6.2d. These molecules are called molecular rectifiers.<sup>11–16</sup>

A strategy combining some of the approaches described above for reducing charge recombination, is the introduction of charge separating dyes that are commonly used on the other half-cell reaction, the photodriven hydrogen evolution on the photocathode.<sup>17–19</sup> They consist of  $\pi$ -conjugated donor-acceptor molecules, with a donor component that accumulates hole density, an acceptor that accumulates electron density and a  $\pi$ -system bridging the two. This arrangement of donor –  $\pi$  system – acceptor (DON- $\pi$ -ACC) is often also called a push-pull system, named after their respective properties of pushing (donor) or pulling (acceptor) electron



density.<sup>20,21</sup> The electronic properties of these systems are designed to allow for efficient intramolecular charge transfer. The explicit molecular systems can vary quite significantly, depending on the requirements on the molecules in their device implementation. Within the context of DSSCs and DS-PECs, some common donor molecules include diphenylamines (DPA)<sup>17,18,20,22</sup> and triphenylamines (TPA)<sup>19,23–30</sup> as well as their derivatives<sup>31–33</sup>. The  $\pi$ -conjugated molecular spacer or bridge is often an extended system, such as thiophene derivatives<sup>19,24,27,31,34</sup> or fluorenes.<sup>18,17,20,29–31</sup> The bridge can however also involve a photosensitizer such as porphyrin,<sup>33,25,35</sup> that donates an electron to the acceptor while the hole is transferred to the donor. If either the bridge or the donor is the photosensitizer, the acceptor can be non-photoactive, such as benzoic acids<sup>24,25,33,35</sup>. Cyano acrylic acids<sup>22,31,34</sup> are also used as acceptors, but various fragments can be chosen to tune the desired energy levels.<sup>27</sup> A common photoactive acceptor is perylene-monoimide (PMI).<sup>17–19,29,30</sup> The dyes are often equipped with alkyl or alkoxy chains to act as a protective layer for the respective electrode and anchoring groups, preventing electrolyte interference, but also dye aggregation.<sup>17–19,24,31,33,35</sup>

Implemented within a larger donor-acceptor system, these dyes can act as barrier, bridge or molecular rectifier, for either electron or hole, allowing for easy transfer in one direction, while inhibiting back transfer. Organic molecules with these charge separating qualities are therefore of interest in both half cells of DS-PECs whenever charge recombination becomes a major loss pathway.

Here, we do an *in silico* investigation and optimization of such push-pull systems for efficient charge separation and back-transfer suppression using a quantum-classical semi-empirical approach: GFN-xTB<sup>36</sup> based nuclear classical dynamics in the ground state are followed by an AO/MO quantum propagation of photoexcited electron and hole on these nuclear trajectories using an extended Hückel Hamiltonian.<sup>37,38</sup> GFN-xTB has been optimized for geometries and frequencies and has proven reliable in a wide variety of systems.<sup>39–43</sup> The general trends that can be extracted from this investigation should help to optimize charge separating



components for other systems as well, such as the dye-WOC complexes in the photoanode of a DS-PEC.

The structure of the investigated dyes is as follows: a Perylene Mono Imide (PMI) derived fragment acts as acceptor and photosensitizer. It is connected via a fluorene-based bridge (FLU) to a polyphenyl amine donor, here for example a triphenyl amine (TPA) with carboxylic acid groups. These organic molecules are based on charge separating dyes first synthesized and tested by Liu *et al.*<sup>17,18</sup> A schematic of the energetics obtained experimentally from Cyclic Voltammetry (CV) and UV-Vis experiments<sup>44</sup> of the involved fragments is shown in Figure 6.3.

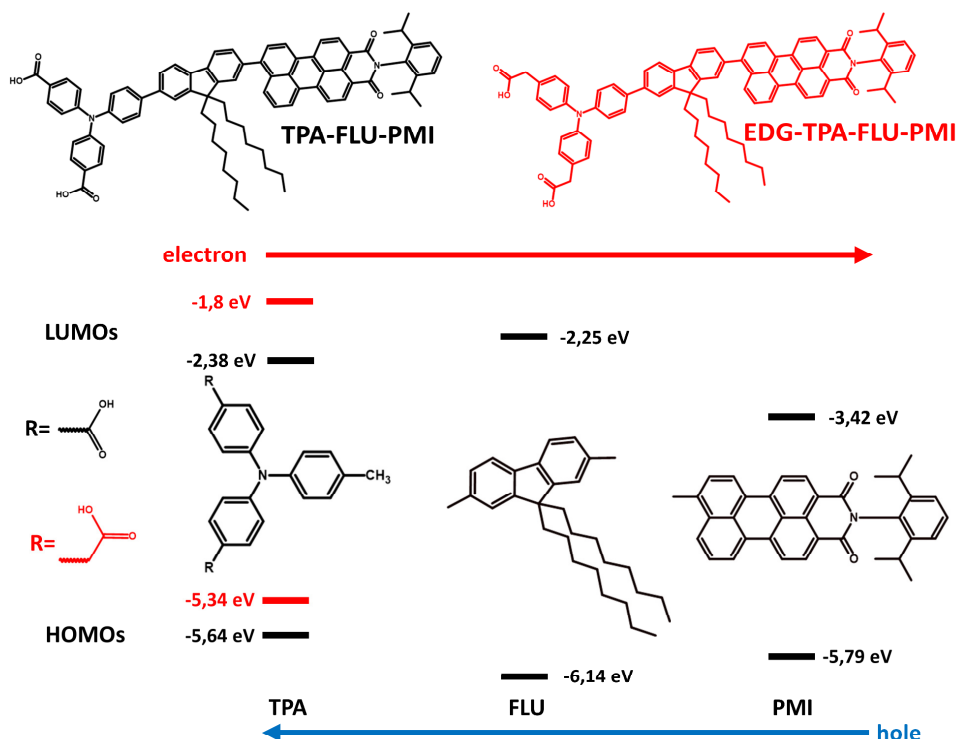


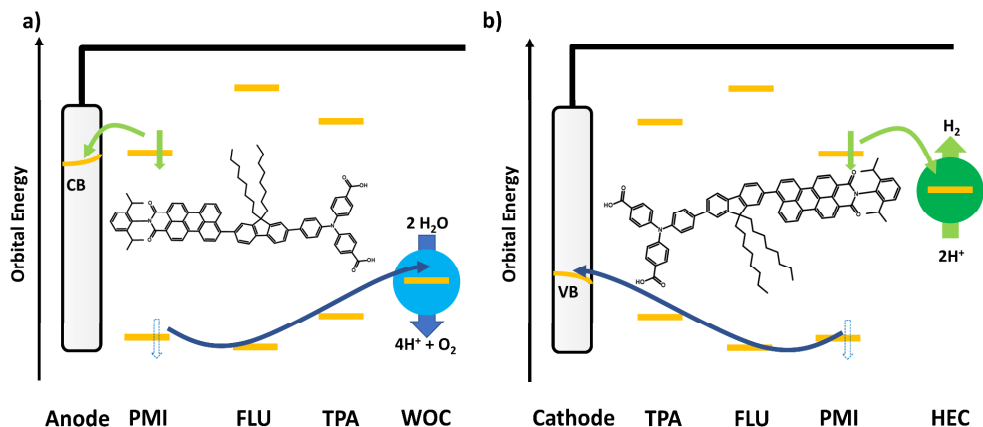
**Figure 6.3.** Molecular fragments of the TPA-FLU-PMI charge separating dye (chemical structure on top, black) with orbital energy levels obtained through experimental CV and UV-Vis redox potentials.<sup>44</sup> Due to the higher HOMO energy of the TPA fragment, the hole moves towards the TPA, while the electron moves towards the PMI. Exchanging the COOH groups of the TPA by CH<sub>2</sub>COOH (red, EDG-TPA) leads to the EDG-TPA-FLU-PMI dye



(chemical structure on top in red) with a larger driving force for both the electron to move towards the PMI and the hole to move towards the EDG-TPA (red).

Due to the gradient in energy from the donor to the acceptor part of the molecule, the excited electron moves towards the acceptor, while the hole moves towards the polyphenyl amine donor.

The fluorene acts as both a bridge for the hole and as a barrier for the electron to prevent electron density from moving towards the donor. The electron can then be picked up by an oxidative agent, as *e.g.* on the photoanode side by the  $\text{TiO}_2$  electrode, or on the photocathode by a hydrogen evolution catalyst (HEC) as shown in scheme 6.1. The hole is either injected from the donor into a semiconductor cathode or, for example, used to drive a water oxidation catalyst (WOC) on the photoanode side.



**Scheme 6.1.** Potential use of a charge separating dye in the context of a DS-PEC: **a)** on the photoanode side, where the photoexcited PMI donates the electron (green) into the CB of the anode, the hole (blue) is transferred via the FLU and TPA to a WOC to oxidize water, **b)** on the photocathode side, where the photoexcited PMI donates the electron (green) to a suitable HEC for hydrogen evolution, while the hole (blue) is transferred via FLU and TPA to be injected into the valence band (VB) of a suitable cathode.

Several strategies are tested to increase the charge separation efficiency of these dyes. Increasing the driving force between donor and acceptor should increase the charge separation efficiency. A comparison is therefore performed between two different donors with different energy levels: a diformate triphenyl amine group on

192



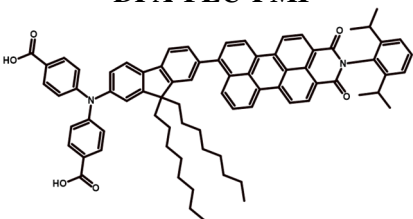
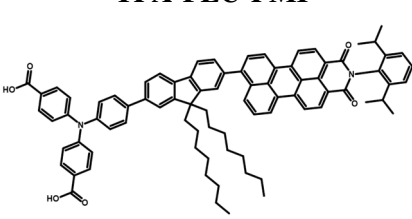
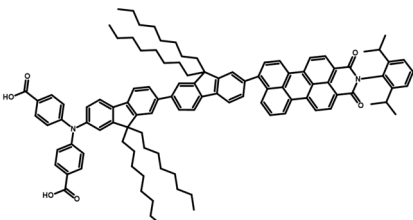
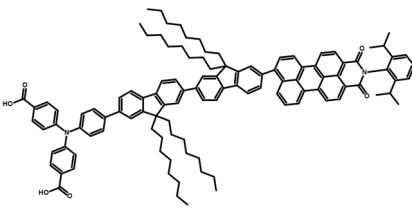
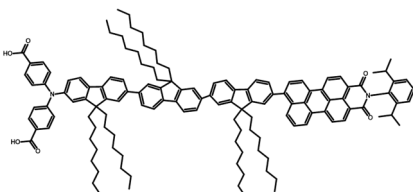
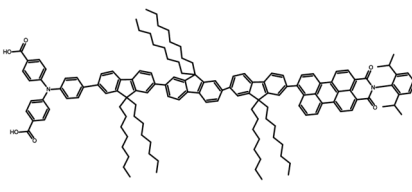
the TPA is exchanged by two acetate groups to change from an electron withdrawing substituent to an electron donating group (EDG-TPA), with the effect of a higher HOMO energy (see figure 6.3). This increase in driving force between the HOMO of the TPA and HOMO of the PMI should result in a larger polarization of the molecule, since more hole density should reside on the donor side.

However, since the donor as well as the acceptor part of the charge separating dyes might already have tuned energetic alignment with their respective reaction partners for further electron and hole transfer, it is also relevant to find ways to optimize these charge separating dyes without changing the energy levels of the donor and acceptor part of these molecules. Several different strategies are followed to obtain a better charge separation without increasing the driving force significantly. As mentioned before, here we use the triphenyl amine (TPA) as a donor. While the fluorene-PMI based dyes introduced by Liu *et al.* included a diphenylamine (DPA) donor<sup>17,18</sup>, other successful push-pull systems were introduced with a TPA.<sup>19,26,28</sup> To estimate which donor would be more efficient in these systems, the effect of a DPA/TPA donor is investigated.

As the fluorene bridge acts as a spatial separation of the donor and acceptor, increasing the bridge length should have a relevant impact on the hole transfer dynamics, as has been shown experimentally in similar molecular systems.<sup>18,19</sup> Therefore, a further investigation of the effect of the number of fluorene bridge molecules on the charge separation is performed. The investigated dyes, including dyes with both DPA and TPA donors and one, two or three fluorene fragments, are given in table 6.1 including the nomenclature used throughout the chapter.



**Table 6.1.** Chemical structures and nomenclature used of the charge separating dyes, with different donors, triphenylamine (TPA) and diphenylamine (DPA), as well as increasing number of fluorenes in the bridge.

	Diphenylamine (DPA) donor	Triphenylamine (TPA) donor
1 fluorene	<p><b>DPA-FLU-PMI</b></p> 	<p><b>TPA-FLU-PMI</b></p> 
2 fluorenes	<p><b>DPA-2FLU-PMI</b></p> 	<p><b>TPA-2FLU-PMI</b></p> 
3 fluorenes	<p><b>DPA-3FLU-PMI</b></p> 	<p><b>TPA-3FLU-PMI</b></p> 

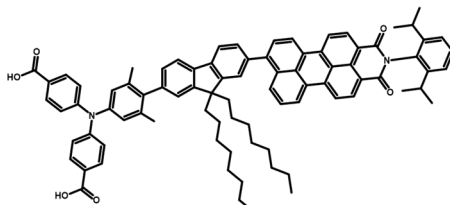
Finally, the close coupling between the different components of the charge separating dye diminishes the triad character of the dye, with the hole flowing freely between the different components, lowering the charge separation efficiency. To decrease the coupling between the components and reduce the back transfer of hole density towards the PMI, methyl groups are introduced to keep dihedral angles close to 90 degrees. In table 6.2, chemical structures of the sterically decoupled molecules are given, with the nomenclature used in the rest of the chapter.



**Table 6.2.** Chemical structures and nomenclature used throughout the chapter of investigated, decoupled dyes. The conjugation of the extended pi-systems is broken by introducing sterically demanding methyl groups to enforce approximately perpendicular dihedral angles on the TPA (TPAMe-FLU-PMI), the fluorene (TPA-FLUMe-PMI) or the PMI (TPA-FLU-PMIMe).

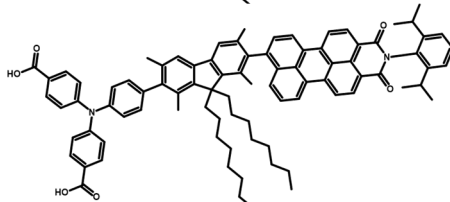
Methylated TPA:

**TPAMe-FLU-PMI**



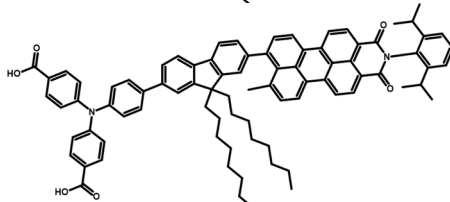
Methylated FLU:

**TPA-FLUMe-PMI**



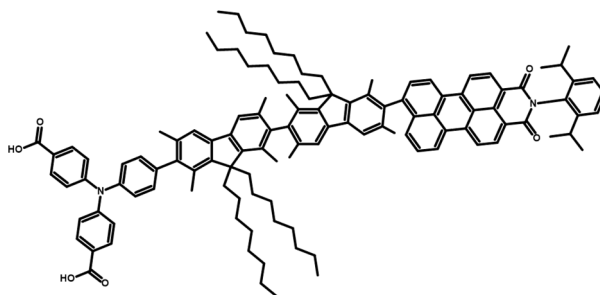
Methylated PMI:

**TPA-FLU-PMIMe**



Our *in silico* investigation finds that the EDG-TPA donor increases charge separation efficiency in comparison to the TPA donor. TPAs give a larger spatial separation between electron and hole than DPAs, while the increasing chain length of fluorenes increases the separation efficiency up to two fluorenes, while adding a third fluorene does not significantly improve the charge separation, as measured by the equilibrium hole distributions. Introducing methyl groups to decouple the different fragments is most efficient when used on the fluorene bridge. Based on these results we propose an optimized dye that includes the TPA donor connected to the PMI via a bridge that contains two fluorenes, equipped with methyl groups to decouple the fragments. The proposed molecule is shown in scheme 6.2. This molecule shows indeed promise in a more efficient charge separation. The results obtained here are relevant for the optimization of charge transfer processes using push-pull systems for both photodriven water oxidation and hydrogen evolution.





**Scheme 6.2.** Proposed optimized charge separating dye (TPA-2FLUMe-PMI): the TPA donor leads to a larger hole density on the donor in comparison to the fluorenes, the chain length of two fluorenes has been shown to give a more efficient charge separation, while the methyl groups on the fluorene molecules break conjugation, lowering the back transfer of hole density to the PMI.

## 6.2 Computational Methods

### *General Procedure*

Simulations of photoinduced charge separation in these molecular dyes were performed by a combination of the semi-empirical GFN-xTB<sup>36</sup> approach to generate *a priori* classical nuclear trajectories and quantum dynamics simulations of the photoexcited electron and hole using the AO-MO propagator and an extended Hückel Hamiltonian.<sup>37,38,45</sup> Details of this method can be found in chapters 2 and 4. DFT and GFN-xTB based calculations were performed using the DFTB and ADF engines of the AMS2020 program package developed by SCM.<sup>46–49</sup> The quantum propagation was performed using the program developed by Rego and Batista.<sup>37</sup>

### *GFN-xTB-based Molecular Dynamics*

The semi-empirical tight binding approach GFN-xTB was used to generate the nuclear trajectories. An equilibration run with a total simulation time of 15 ps in the NVT ensemble was performed using a Berendsen thermostat<sup>50</sup> at 293.15 K and a time step of 1 fs. This was followed by a MD production run in the NVE ensemble, with a total simulation time of 5 ps, and a time step of 0.1 fs. This trajectory was cut into 10 slices of 500 fs each. Those trajectories were then used in the charge transfer dynamics (CTDs).



### *Optimization of Extended Hückel Parameters*

The extended Hückel parameters were optimized to reproduce experimental redox potentials. For this, geometry optimizations of the different molecular fragments were performed using both GFN-xTB and DFT. For the DFT optimizations, the B3LYP XC-functional<sup>51,52</sup> with a TZP basis set<sup>53</sup> and D3 dispersion corrections with BJ-damping,<sup>54</sup> were used. Both GFN-xTB and DFT lead to comparable geometries, with deviations mostly in the long, flexible alkyl chains. An example is shown for the TPA-FLU-PMI dye in figure 6A.1 in the appendix. The GFN-xTB geometries were used for the parameter optimization, while the DFT results were used for determining the spatial distribution of relevant orbitals. The experimental redox potentials were taken from a manuscript currently in preparation.<sup>44</sup> They were determined via Cyclic Voltammetry and, in cases where the reduction potential was out of measurable bounds, via the main absorption peak onset, which is commonly used to determine reduction potentials.<sup>55,56</sup> Conversion of these potentials to energies in eV of the frontier orbitals is done by following equation 6.1 and 6.2 for the oxidation potential/HOMO and reduction potential/LUMO, respectively. The target HOMO and LUMO energies  $\epsilon_{\text{MOL}}^{\text{HOMO}}$ ,  $\epsilon_{\text{MOL}}^{\text{LUMO}}$  can be estimated from these standard Redox Potentials versus NHE  $E_{\text{ox,NHE}}^0$ ,  $E_{\text{red,NHE}}^0$  with the use of the Faraday constant  $F = N_A * e$  as given in equations 6.1 and 6.2:

$$\epsilon_{\text{MOL}}^{\text{HOMO}} \approx -E_{\text{ox,vacuum}}^0 * nF = -(E_{\text{ox,NHE}}^0 + 4.44 \text{ V}) * e \quad (6.1)$$

$$\epsilon_{\text{MOL}}^{\text{LUMO}} \approx -E_{\text{red,vacuum}}^0 * nF = -(E_{\text{red,NHE}}^0 + 4.44 \text{ V}) * e \quad (6.2)$$

Here  $E_{\text{ox,vacuum}}^0$  and  $E_{\text{red,vacuum}}^0$  are the oxidation and reduction potential versus an electron at rest in vacuum,  $n$  the moles of electrons (here one electron, thus  $\frac{1}{N_A}$ ),  $N_A$  the Avogadro constant and  $e$  the elemental charge. The resulting energies are then in units of eV. The determined target values can be found in table 6A.1 in the appendix. The optimization of the extended Hückel parameters was performed on the GFN-xTB geometries, so that the HOMO/LUMO energies of the respective molecules represent the target values determined in equations 6.1 and 6.2, while the spatial form



of the frontier orbitals was checked against the DFT results, to ensure that the obtained orbitals are physically meaningful. The procedure itself is based on a genetic algorithm described elsewhere.<sup>57</sup> The optimized energies can be found in table 6A.1, the spatial distribution of the frontier orbitals in table 6A.2 in the appendix. After optimization of the different fragment molecules on their experimental redox potentials, the TPA-FLU-PMI and EDG-TPA-FLU-PMI dyes gave remarkably close results to experiment without further optimization (see table 6A.1 in the appendix). For the methylated molecules, the parameters were not reoptimized as there is no corresponding experimental data available; however, the influence on the energies due to this small structural change is expected to be small.

### *Determination of Relevant Excitations*

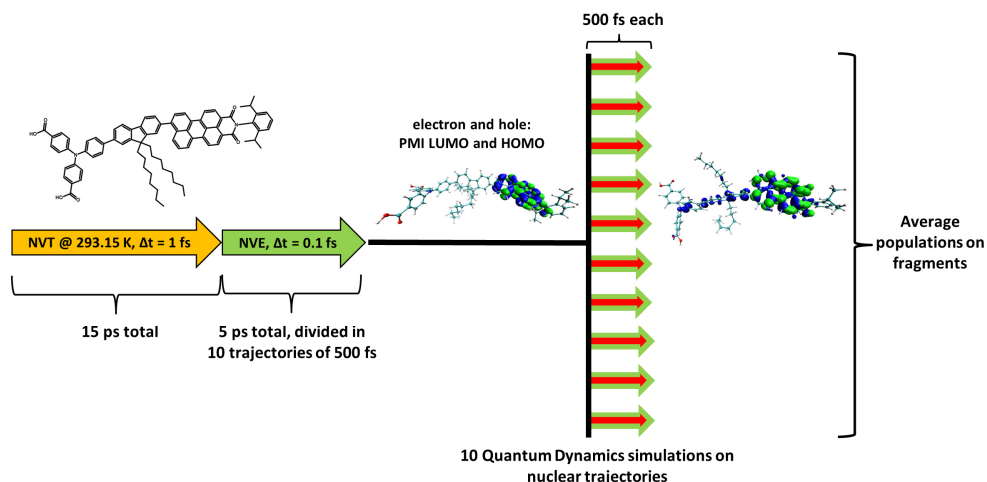
Relevant excitations in the 400-600 nm wavelength range were determined using LR-TDDFT. The long-range corrected hybrid functional camy-B3LYP as implemented in ADF<sup>58-60</sup> was used for all LR-TDDFT simulations, with a DZP basis, a small frozen core and D3-dispersion with BJ-damping. Excitation energies, oscillator strength and transition densities are given in tables 6A.5-6A.15 in the appendix. For all investigated molecules, the excitonic PMI HOMO-LUMO excitation was the most relevant due to its high oscillator strength and excitation energy in the visible light range.

### *Charge Transfer Dynamics*

Simulations of Charge Transfer Dynamics (CTD) were performed on the pre-calculated nuclear trajectories. For each molecule, ten nuclear trajectories of 500 fs length with a time step of 0.1 fs were used, obtained as explained above and shown in scheme 6.3. Two wave packets representing photoexcited electron and hole were chosen based on the LR-TDDFT results: since in all cases, the excitonic PMI excitation is the most relevant in the visible region, the wave packets were prepared as the HOMO and LUMO of the PMI fragment. The wave packets were propagated



on these *a priori* nuclear trajectories, with a time step of 0.1 fs for the electronic propagation. After the CTDs, the populations of electron and hole on the different fragments over time were averaged over the 10 trajectories. The changes of charge over time were obtained by subtracting the electron populations from the hole population on each fragment. Average charges are determined over all CTDs and the last 200fs. since at that point the charges were stabilized in most simulations, and in this way quantitative measures of charge separation efficiencies were obtained. These results are collected for the fragments of all investigated dye molecules in table 6A.16 in the appendix. A representation of the full process of nuclear trajectory generation and CTDs is given in scheme 6.3.



**Scheme 6.3.** Preparation of the nuclear trajectories and production of the CTDs. A 15 ps NVT equilibration run at 293.15 K is followed by a 5 ps long NVE run with a time step of 0.1 fs. This long trajectory is cut into 10 trajectories of 500 fs each in order to sample different initial conditions for the CTDs. On these nuclear trajectories, quantum propagation of electron and hole, represented by the PMI fragment LUMO and HOMO respectively is performed. From these 10 CTD runs, the populations of electron and hole on the respective molecular fragments is averaged to obtain the charge separation within the dye molecule.



### 6.3 Results

The photoinduced charge separation in the push pull system over time is shown for the TPA-FLU-PMI case in figure 6.4, where the charge corresponds to the hole minus electron population for the different fragments. The lines represent the mean average over the ten CTDs, while the shaded area represents the standard deviation.

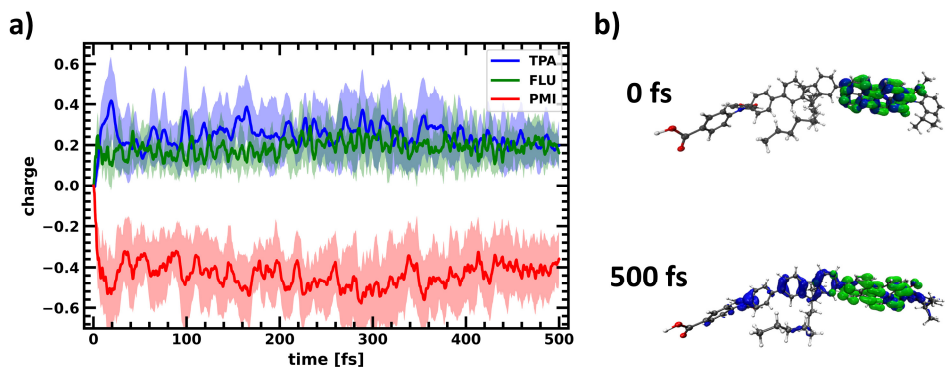


**Figure 6.4.** **a)** Charge separation in the TPA-FLU-PMI dye. Charges are determined as difference between hole and electron population on the respective fragments PMI (red), FLU (green) and TPA (blue). The lines denote mean averages over 10 trajectories, the shaded areas the standard deviation. **b)** electron (green) and hole (blue) densities at the beginning and end of one quantum dynamics trajectory.

Upon photoexcitation, both electron and hole reside on the PMI since the excitation is purely excitonic in character. Thus, the charge difference is initially zero on all fragments. Upon time evolution, the hole migrates to the fluorene and the TPA, while the electron stays at the PMI (see figure 6A.2 in the appendix), resulting in a negative charge accumulating on the PMI, while the FLU and TPA get positively charged. While the initial charge separation is relatively fast, the charges equilibrate after around 200 fs. In addition, hole transfer is not complete, most likely due to the delocalized character of the HOMO (see table 6A.4 in the appendix), and the nearly degenerate lower lying orbitals. Energetic separation is much larger for the unoccupied orbitals (figure 6.3). After the system reaches equilibrium, the average charge on the PMI corresponds to about -0.44, while the FLU obtains a



charge of approximately +0.20 and the TPA of +0.24, based on averaging over the last 200 fs. The TPA-FLU-PMI dye does show photoinduced charge separation, however to an extent that could be further improved.

### *Changing the Driving Force: TPA-FLU-PMI vs EDG-TPA-FLU-PMI Dye*

Experimental work showed an increase in photoinduced hole injection when changing the donor from TPA to EDG-TPA by about 30 %.<sup>44</sup> In figure 6.5, we compare the charge separation over time of the PMI and TPA-derived fragments of the two dyes TPA-FLU-PMI and EDG-FLU-PMI. Here, the FLU has been omitted for clarity. (see table 6A.16 in the appendix).

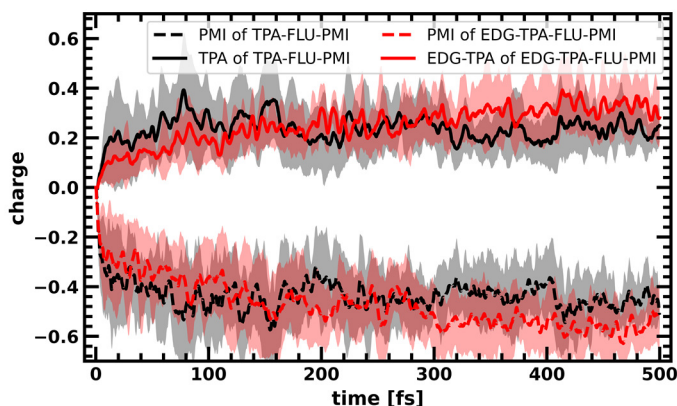


**Figure 6.5.** Charge separation in the TPA-FLU-PMI (black) and EDG-TPA-FLU-PMI (red) dyes. Charges are determined as difference between hole and electron population on the respective fragments PMI (dashed lines) and TPA (solid lines). The lines denote mean averages over 10 trajectories, the shaded areas the standard deviation.

The charge transfer dynamics of the EDG-TPA-FLU-PMI dye is qualitatively similar to the TPA-FLU-PMI, which reflects the close relation between the two dyes. Again, the excitonic excitation of the PMI leads to a neutral charge on all fragments at  $t=0$ . Upon time evolution, hole density is transferred towards the EDG-TPA via the FLU. While the initial charge transfer is delayed in comparison to the TPA-FLU-PMI, more hole density is transferred from the PMI to the EDG-TPA over time. Equilibration is also reached at a later stage. This decrease in initial charge separation



is most likely due to the less delocalized HOMO (see table 6A.4) of the EDG-TPA-FLU-PMI compared to the TPA-FLU-PMI, with weaker coupling between the PMI and EDG-TPA fragments. However, after the initial slow down, the larger driving force and spatial localization of the HOMO on the EDG-TPA leads to a stronger polarization compared to the TPA-FLU-PMI, as more hole density resides on average at the donor. When comparing the time average of the charge from the 300 fs mark on, where equilibrium appears to be achieved and the red and black curve clearly cross each other (see Figure 6.5), the EDG-TPA-FLU-PMI shows a significantly increased charge separation relative to the TPA-FLU-PMI: while the PMI had a charge of -0.43 in the TPA-FLU-PMI dye, this decreases to approximately -0.53 for the EDG-TPA-FLU-PMI dye. The positive charge of about +0.23 in the TPA is increased to an approximate value of 0.30 for the EDG-TPA, while the charge on the FLU increases a little less (+0.20 vs. +0.23). This points to a more efficient charge separation. The electron donating character of the methylene groups pulls the HOMO towards the EDG-TPA and increases its energy, leading to a larger driving force for the hole to move towards the donor. While dynamic disorder causes fluctuations in the orbital energies and therefore also to oscillations in hole population on the different fragments due to alternating forward and back transfer, the average hole population on the donor is increased in comparison to the TPA-FLU-PMI. This larger separation of electron and hole results in a lower charge recombination probability due to the lower spatial overlap of electron and hole densities for the EDG-TPA based dye than for the dye using a TPA donor. These findings are in line with the experimentally determined increased hole lifetimes for the EDG-TPA-FLU-PMI dye in comparison to the TPA-FLU-PMI.<sup>44</sup>



### *DPA vs TPA Donor*

Introducing a TPA or DPA has little effect on the driving force in these charge separating dyes, as the HOMO energies are similar. This is supported by the density of states of these two fragments (figure 6.6). The peaks denoted HOMO ( $\sim -11.6$  eV) and LUMO ( $\sim -8.4$  eV) have almost the same energy for the two systems. Therefore, the boundary condition of a similar donor HOMO energy remains fulfilled when exchanging DPA and TPA.

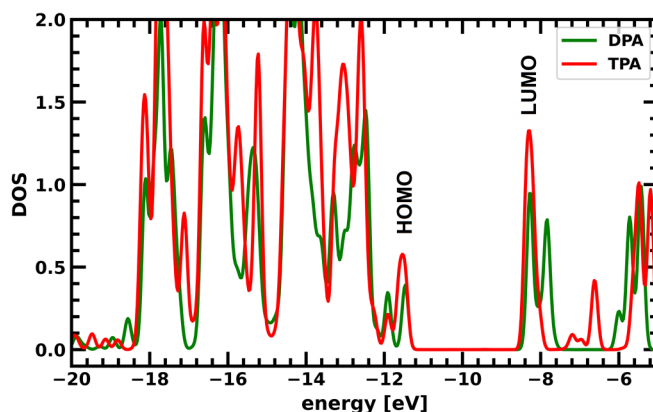


**Figure 6.6.** Partial Density Of States (PDOS) of the TPA (red) and DPA (green) donors.

A comparison between the TPA-FLU-PMI and DPA-FLU-PMI charge separation efficiency in the form of net charge on the PMI after photoexcitation is shown in figure 6.7a. Here, the other fragments as well as the standard deviation are omitted, the traces represent averages over 10 CTD simulations. The initial charge separation is slightly delayed with the DPA donor compared to the TPA as donor; however, this difference diminishes after around 100 fs. When averaging over the last 200fs, the charge on the PMI is -0.46 and -0.44 for the DPA-FLU-PMI and TPA-FLU-PMI dyes, respectively. While the charge on the PMI is not significantly changed, the TPA leads to a further polarization with a higher positive charge on the donor (+0.24) and lower on the fluorene (+0.20) in comparison to the DPA based dyes (+0.20 and +0.26 for DPA and FLU, respectively) as seen in figure 6.7b. This holds true also



when comparing the DPA-2FLU-PMI with the TPA-2FLU-PMI molecules (see figure 6A.3 and table 6A.16 in the appendix).

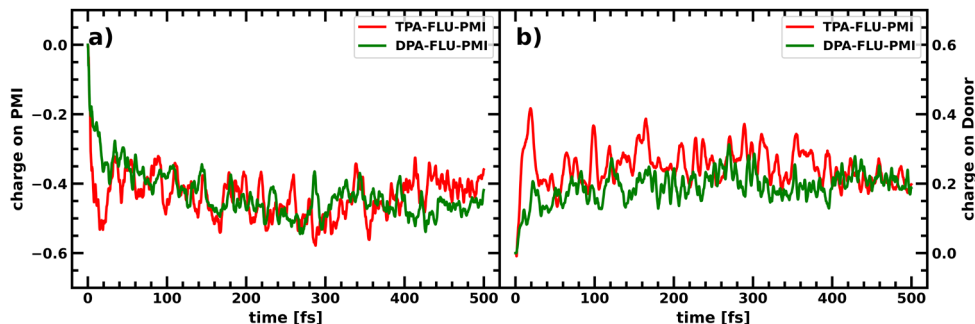


**Figure 6.7.** **a)** Average charge accumulation averaged over 10 CTDs on the PMI in the TPA-FLU-PMI (red) and DPA-FLU-PMI (green) dyes upon photoexcitation of the PMI. **b)** Average charge accumulation averaged over 10 CTDs on the donor (TPA/DPA) in the TPA-FLU-PMI (red) and DPA-FLU-PMI (green) dyes upon photoexcitation of the PMI.

While the same amount of hole density is transferred from the PMI, the charge separation is more efficient using a TPA instead of a DPA donor molecule: the TPA leads to larger polarization, as more hole density accumulates on the TPA instead of the FLU. For an efficient spatial separation, TPAs as donors are preferred.

### *Increasing the Bridge Length*

In figure 6.8, the change in charge on each fragment of the charge separating dyes over time is shown for the TPA-XFLU-PMI and DPA-XFLU-PMI molecules, with the number of FLU fragments X changing from 1 to 3. While increasing the chain length from one fluorene to two fluorene molecules increases the charge separation efficiency significantly for both the TPA and DPA based dyes, introducing a third fluorene does not increase the charge separation any further for the TPA based dye, while the DPA-3FLU-PMI dye shows an initially better performance than the DPA-2FLU-PMI dye that diminishes after around 300 fs (see also table 6A.16 in the appendix).



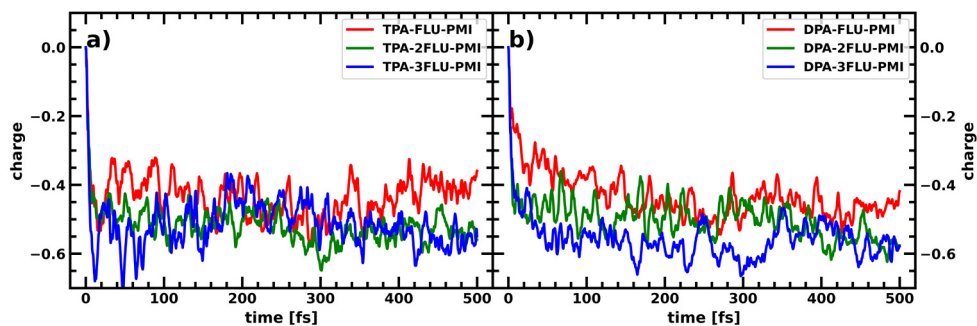


**Figure 6.8.** Average charge accumulation averaged over 10 CTDs on the PMI with increasing fluorene spacer bridge upon photoexcitation of the PMI: **a)** in the TPA-FLU-PMI (red), TPA-2FLU-PMI (green) and TPA-3FLU-PMI dyes. **b)** in the DPA-FLU-PMI (red), DPA-2FLU-PMI (green) and DPA-3FLU-PMI dyes.

Experimentally, an increase of fluorene chain length has been shown to increase the performance of the DPA-XFLU-PMI dyes (differing only in alkyl chain length), with the DPA-2FLU-PMI dye showing the best performance.<sup>18</sup> Our computational results also suggest that the charge separation efficiency does not significantly increase when moving from 2 fluorene bridges to using 3 fluorenes, since the hole mainly accumulates on the additional fluorenes with limited hole density on the donor (see table 6A.15 in the appendix). Liu et al. attribute the lower efficiency of DPA-3FLU-PMI in a photocathode to a lower loading of the molecule on the electrode in comparison to the DPA-FLU-PMI and DPA-2FLU-PMI molecules.<sup>18</sup> However, another influence on the decreased performance of the DPA-3FLU-PMI and TPA-3FLU-PMI molecules in comparison to their counterparts with one or two fluorenes might also be their different absorption behavior. With increasing fluorene length, the fluorene based excitonic excitation lowers in energy and increases in oscillator strength, becoming slightly competitive to the PMI based excitation as shown in figure 6A.4 in the appendix, also in agreement with experimental UV-VIS results.<sup>18</sup> A fluorene-based excitation leads to electron transfer towards not only the PMI but also the donor (TPA or DPA), increasing the likelihood of charge recombination.

All in all, increasing the chain length from one to two fluorene molecules leads to improved performance, while a three-fluorene bridge does not improve the charge



separation efficiency further and allows for competing pathways through the excitation of the fluorenes, that lead to recombination instead of charge separation, lowering the overall efficiency.

### *Decoupling the Fragments*

One of the problems in the photoinduced charge separation process of these dyes is the relative delocalization of the molecular HOMO, as well as the nearly degenerate states, leading to a spread out of the hole. One approach to increase the average hole population on the donor is by increasing the driving force, pulling the hole towards the donor. Another possibility however would be to limit delocalization of the HOMO to the donor fragment, by decoupling the different fragments of the molecular dye. This can be achieved by breaking the conjugation between the different components, by forcing the dihedral angle towards a perpendicular orientation and thereby separating the fragments molecular orbitals from one another. Photoinduced charge separation should then still be possible, since dynamic fluctuations should also lead to changes in the dihedrals, allowing charge flow for certain nuclear conformations. While this might slow down initial charge transfer, it should lead to a distinct separation of fragment states, with the HOMO localized on the donor, reducing delocalization of the hole over the entire molecule and suppressing back transfer. The inclusion of methyl groups can help enforcing a near perpendicular arrangement of the fragment's  $\pi$ -systems, by introducing steric strain. Methyl groups were therefore introduced on different parts of the molecule to study the effect on the charge separation process. In figure 6.9, charge transfer within the dye is visualized through the net charge over time on the PMI fragment for the original TPA-FLU-PMI dye in comparison to dyes equipped with methyl groups at each respective fragment to break conjugation: TPAMe-FLU-PMI, TPA-FLUMe-PMI and TPA-FLU-PMIMe.



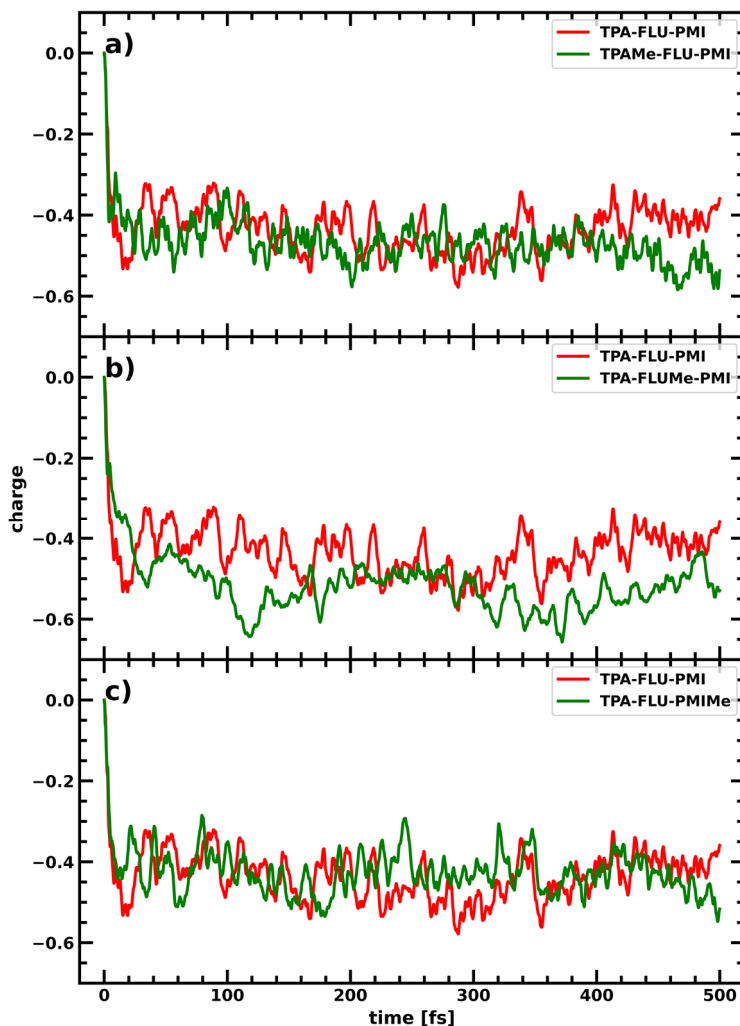


**Figure 6.9.** Average charge accumulation averaged over 10 CTDs on the PMI in the TPA-FLU-PMI case (red) compared to the respective methylated derivatives in green: **a)** TPAMe-FLU-PMI, **b)** TPA-FLUMe-PMI, **c)** TPA-FLU-PMIMe.

While a methyl group on the PMI does not lead to further hole transfer towards fluorene and TPA than for the TPA-FLU-PMI molecule, breaking the conjugation through methyl groups on the TPA and FLU leads to a lower net charge on the PMI (see table 6A.15 in the appendix), thus increasing charge separation in comparison to the planar molecule. Introducing methyl groups to the fluorene seems most promising, since more hole density is transferred to TPA and FLU, which is not



surprising since methyl groups on the FLU keep both dihedral angles at approximately 90 degrees. However, larger fluctuations are observable than for the coupled case. The charge separation process in the TPA-FLU-PMI dye becomes much more sensitive towards the respective nuclear conformation in comparison to the non-methylated dyes. Decoupling the fragments from another by breaking conjugation through dihedral angles of roughly 90 degrees can therefore increase the charge separation efficiency.

### *In Silico Optimization of Charge Separating Dyes*

The results presented in the sections above of this systematic *in silico* investigation of effect of TPA vs. DPA donors, increasing the bridge length and decoupling the fragments can be used to guide the optimization of these fluorene/PMI based charge separating dyes. As the TPA resulted in more positive charge accumulation on the donor part than for the DPA, the TPA was chosen as the donor. Two fluorene molecules were chosen as bridge, as suggested by the results on optimal fluorene chain length. To decouple the different components and suppress the hole back transfer, these two fluorenes were equipped with methyl groups to keep the dihedral angles between all fragments of the molecular system close to 90 degrees, decoupling them and refining the different orbitals, keeping them localized. The resulting net charge evolution over time on the PMI averaged over 10 CTD trajectories is shown in figure 6.10.



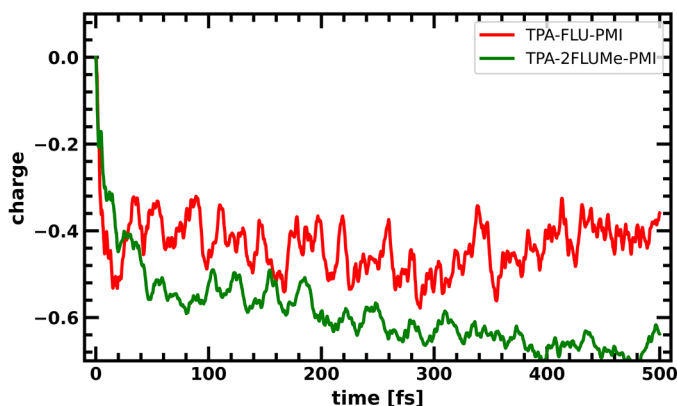


**Figure 6.10.** Average charge accumulation averaged over 10 CTDs on the PMI in the TPA-FLU-PMI (red) and the optimized TPA-2FLUMe-PMI (green) dye.

The combination of all of the modular optimizations of the different components of the dye (TPA donor, 2 fluorenes, decoupling through methyl groups) has led to a significantly enhanced charge separation. While the original TPA-FLU-PMI dye equilibrates to a charge of about -0.44 for the PMI, in the optimized TPA-2FLUMe-PMI dye, equilibrium was not yet reached yet after 500 fs, with the average charge on the PMI at -0.66 with a further negative tendency. Overall, combining the different strategies tested before, resulted in a dye optimized *in silico* that shows an impressive increase of charge accumulation by about 50% relative to the TPA-FLU-PMI.

### 6.4 Conclusion

Systematic investigations of phenylamine-fluorene-PMI based charge separating dyes were done on a semi-empirical quantum classical level to estimate the charge separation efficiency in this family of push-pull dyes. We find that exchanging the electron withdrawing character of the COOH substituent on the TPA by introducing an electron donating methylene group between the phenyl and carboxylic acid groups, the increased HOMO energy level and its localization on the donor side leads



to a more efficient charge separating dye with lower recombination rates, as confirmed by experiment. We also find that TPA donors lead to a more polarized charge transfer state than for their DPA relatives and should therefore be preferred. An increased bridge length between donor and acceptor from one fluorene fragment to two, leads to a better charge separation, however this effect decreases when expanding this to three fluorene fragments. Additionally, fluorene-based transitions shift towards the visible range, becoming more competitive with the desired PMI based excitation. Decoupling of the different components in the dyes by sterically demanding methyl groups is an effective way of decreasing back transfer and therefore decreasing the chance of recombination. This is most effective when used on the fluorene. The insight gained from these investigations were then used to propose an *in silico* optimized charge separating dye using a TPA donor, a bridge of two methylated fluorenes and a PMI acceptor. This dye showed remarkable enhancement in charge separation efficiency, with an increase of negative charge by about 50% on the PMI in comparison to the original TPA-FLU-PMI dye. The results gained from this *in silico* investigation and optimization of charge separating dyes should help in guiding experimental work on improving these molecules, to lower charge recombination and increase device efficiency.



## 6.5 References

- (1) Yu, Z.; Li, F.; Sun, L. Recent Advances in Dye-Sensitized Photoelectrochemical Cells for Solar Hydrogen Production Based on Molecular Components. *Energy Environ. Sci.* **2015**, *8* (3), 760–775. <https://doi.org/10.1039/C4EE03565H>.
- (2) Shao, Y.; de Ruiter, J. M.; de Groot, H. J. M.; Buda, F. Photocatalytic Water Splitting Cycle in a Dye-Catalyst Supramolecular Complex: Ab Initio Molecular Dynamics Simulations. *J. Phys. Chem. C* **2019**, *123* (35), 21403–21414. <https://doi.org/10.1021/acs.jpcc.9b06401>.
- (3) Monti, A.; de Ruiter, J. M.; de Groot, H. J. M.; Buda, F. A Dynamic View of Proton-Coupled Electron Transfer in Photocatalytic Water Splitting. *J. Phys. Chem. C* **2016**, *120* (40), 23074–23082. <https://doi.org/10.1021/acs.jpcc.6b08244>.
- (4) Bell, T. D. M.; Pagba, C.; Myahkostupov, M.; Hofkens, J.; Piotrowiak, P. Inhomogeneity of Electron Injection Rates in Dye-Sensitized TiO<sub>2</sub>: Comparison of the Mesoporous Film and Single Nanoparticle Behavior. *J. Phys. Chem. B* **2006**, *110* (50), 25314–25321. <https://doi.org/10.1021/jp064005f>.
- (5) Duan, L.; Bozoglian, F.; Mandal, S.; Stewart, B.; Privalov, T.; Llobet, A.; Sun, L. A Molecular Ruthenium Catalyst with Water-Oxidation Activity Comparable to That of Photosystem II. *Nature Chem.* **2012**, *4* (5), 418–423. <https://doi.org/10.1038/nchem.1301>.
- (6) Wang, L.; Duan, L.; Wang, Y.; Ahlquist, M. S. G.; Sun, L. Highly Efficient and Robust Molecular Water Oxidation Catalysts Based on Ruthenium Complexes. *Chem. Commun.* **2014**, *50* (85), 12947–12950. <https://doi.org/10.1039/C4CC05069J>.
- (7) Duan, L.; Wang, L.; Li, F.; Li, F.; Sun, L. Highly Efficient Bioinspired Molecular Ru Water Oxidation Catalysts with Negatively Charged Backbone Ligands. *Acc. Chem. Res.* **2015**, *48* (7), 2084–2096. <https://doi.org/10.1021/acs.accounts.5b00149>.
- (8) Zhang, B.; Sun, L. Artificial Photosynthesis: Opportunities and Challenges of Molecular Catalysts. *Chemical Society Reviews* **2019**, *48* (7), 2216–2264. <https://doi.org/10.1039/C8CS00897C>.
- (9) Yang, J.; Wang, L.; Zhan, S.; Zou, H.; Chen, H.; Ahlquist, M. S. G.; Duan, L.; Sun, L. From Ru-Bda to Ru-Bds: A Step Forward to Highly Efficient Molecular Water Oxidation Electrocatalysts under Acidic and Neutral Conditions. *Nat Commun* **2021**, *12* (1), 373. <https://doi.org/10.1038/s41467-020-20637-8>.
- (10) Rochaix, J.-D. Regulation of Photosynthetic Electron Transport. *Biochimica et Biophysica Acta (BBA) - Bioenergetics* **2011**, *1807* (3), 375–383. <https://doi.org/10.1016/j.bbabi.2010.11.010>.
- (11) Aviram, A.; Ratner, M. A. Molecular Rectifiers. *Chemical Physics Letters* **1974**, *29* (2), 277–283. [https://doi.org/10.1016/0009-2614\(74\)85031-1](https://doi.org/10.1016/0009-2614(74)85031-1).
- (12) Bera, A.; Pal, A. J. Molecular Rectifiers Based on Donor/Acceptor Assemblies: Effect of Orientation of the Components' Magnetic Moments. *Nanoscale* **2013**, *5* (14), 6518–6524. <https://doi.org/10.1039/C3NR00493G>.
- (13) Ding, W.; Negre, C. F. A.; Vogt, L.; Batista, V. S. Single Molecule Rectification Induced by the Asymmetry of a Single Frontier Orbital. *J. Chem. Theory Comput.* **2014**, *10* (8), 3393–3400. <https://doi.org/10.1021/ct5004687>.
- (14) Van Dyck, C.; Ratner, M. A. Molecular Rectifiers: A New Design Based on Asymmetric Anchoring Moieties. *Nano Lett.* **2015**, *15* (3), 1577–1584. <https://doi.org/10.1021/nl504091v>.
- (15) Koepf, M.; Koenigsmann, C.; Ding, W.; Batra, A.; Negre, C. F. A.; Venkataraman, L.; Brudvig, G. W.; Batista, V. S.; Schmuttenmaer, C. A.; Crabtree, R. H. Controlling the Rectification Properties of Molecular Junctions through Molecule–Electrode Coupling. *Nanoscale* **2016**, *8* (36), 16357–16362. <https://doi.org/10.1039/C6NR04830G>.
- (16) Ding, W.; Koepf, M.; Koenigsmann, C.; Batra, A.; Venkataraman, L.; Negre, C. F. A.; Brudvig, G. W.; Crabtree, R. H.; Schmuttenmaer, C. A.; Batista, V. S. Computational Design of Intrinsic Molecular Rectifiers Based on Asymmetric Functionalization of N-Phenylbenzamide. *J Chem Theory Comput* **2015**, *11* (12), 5888–5896. <https://doi.org/10.1021/acs.jctc.5b00823>.



- (17) Liu, Z.; Xiong, D.; Xu, X.; Arooj, Q.; Wang, H.; Yin, L.; Li, W.; Wu, H.; Zhao, Z.; Chen, W.; Wang, M.; Wang, F.; Cheng, Y.-B.; He, H. Modulated Charge Injection in P-Type Dye-Sensitized Solar Cells Using Fluorene-Based Light Absorbers. *ACS Appl. Mater. Interfaces* **2014**, 6 (5), 3448–3454. <https://doi.org/10.1021/am405610b>.
- (18) Liu, Z.; Li, W.; Topa, S.; Xu, X.; Zeng, X.; Zhao, Z.; Wang, M.; Chen, W.; Wang, F.; Cheng, Y.-B.; He, H. Fine Tuning of Fluorene-Based Dye Structures for High-Efficiency p-Type Dye-Sensitized Solar Cells. *ACS Appl. Mater. Interfaces* **2014**, 6 (13), 10614–10622. <https://doi.org/10.1021/am5022396>.
- (19) Nattestad, A.; Mozer, A. J.; Fischer, M. K. R.; Cheng, Y.-B.; Mishra, A.; Bäuerle, P.; Bach, U. Highly Efficient Photocathodes for Dye-Sensitized Tandem Solar Cells. *Nature Mater* **2010**, 9 (1), 31–35. <https://doi.org/10.1038/nmat2588>.
- (20) Rémond, M.; Hwang, J.; Kim, J.; Kim, S.; Kim, D.; Bucher, C.; Bretonnière, Y.; Andraud, C.; Kim, E. Push–Pull Dyes for Yellow to NIR Emitting Electrochemical Cells. *Advanced Functional Materials* **2020**, 30 (50), 2004831. <https://doi.org/10.1002/adfm.202004831>.
- (21) Kundu, R.; Kulshreshtha, C. Design, Synthesis and Electronic Properties of Push–Pull–Push Type Dye. *RSC Adv.* **2015**, 5 (94), 77460–77468. <https://doi.org/10.1039/C5RA13416A>.
- (22) Velusamy, M.; Justin Thomas, K. R.; Lin, J. T.; Hsu, Y.-C.; Ho, K.-C. Organic Dyes Incorporating Low-Band-Gap Chromophores for Dye-Sensitized Solar Cells. *Org. Lett.* **2005**, 7 (10), 1899–1902. <https://doi.org/10.1021/ol050417f>.
- (23) Ren, S.; Zeng, D.; Zhong, H.; Wang, Y.; Qian, S.; Fang, Q. Star-Shaped Donor- $\pi$ -Acceptor Conjugated Oligomers with 1,3,5-Triazine Cores: Convergent Synthesis and Multifunctional Properties. *J. Phys. Chem. B* **2010**, 114 (32), 10374–10383. <https://doi.org/10.1021/jp104710y>.
- (24) Zhang, M.; Wang, Y.; Xu, M.; Ma, W.; Li, R.; Wang, P. Design of High-Efficiency Organic Dyes for Titania Solar Cells Based on the Chromophoric Core of Cyclopentadithiophene-Benzothiadiazole. *Energy Environ. Sci.* **2013**, 6 (10), 2944–2949. <https://doi.org/10.1039/C3EE42331J>.
- (25) Chen, J.; Sheng, Y.; Ko, S.; Liu, L.; Han, H.; Li, X. Push–Pull Porphyrins with Different Anchoring Group Orientations for Fully Printable Monolithic Dye-Sensitized Solar Cells with Mesoscopic Carbon Counter Electrodes. *New J. Chem.* **2015**, 39 (7), 5231–5239. <https://doi.org/10.1039/C5NJ00569H>.
- (26) Kaeffer, N.; Windle, C. D.; Brisse, R.; Gablin, C.; Leonard, D.; Joussetme, B.; Chavarot-Kerlidou, M.; Artero, V. Insights into the Mechanism and Aging of a Noble-Metal Free H<sub>2</sub>-Evolving Dye-Sensitized Photocathode. *Chem. Sci.* **2018**, 9 (32), 6721–6738. <https://doi.org/10.1039/C8SC00899J>.
- (27) Brisse, R.; Praveen, C.; Maffei, V.; Bourgeteau, T.; Tondelier, D.; Berthelot, T.; Geffroy, B.; Gustavsson, T.; Raimundo, J. M.; Joussetme, B. A Red to Blue Series of Push–Pull Dyes for NiO Based p-DSSCs. *Sustainable Energy Fuels* **2018**, 2 (3), 648–654. <https://doi.org/10.1039/C7SE00474E>.
- (28) Massin, J.; Bräutigam, M.; Bold, S.; Wächter, M.; Pavone, M.; Muñoz-García, A. B.; Dietzek, B.; Artero, V.; Chavarot-Kerlidou, M. Investigating Light-Driven Hole Injection and Hydrogen Evolution Catalysis at Dye-Sensitized NiO Photocathodes: A Combined Experimental–Theoretical Study. *J. Phys. Chem. C* **2019**, 123 (28), 17176–17184. <https://doi.org/10.1021/acs.jpcc.9b04715>.
- (29) Powar, S.; Daeneke, T.; Ma, M. T.; Fu, D.; Duffy, N. W.; Götz, G.; Weidelener, M.; Mishra, A.; Bäuerle, P.; Spiccia, L.; Bach, U. Highly Efficient P-Type Dye-Sensitized Solar Cells Based on Tris(1,2-Diaminoethane)Cobalt(II)/(III) Electrolytes. *Angewandte Chemie* **2013**, 125 (2), 630–633. <https://doi.org/10.1002/ange.201206219>.
- (30) Weidelener, M.; Mishra, A.; Nattestad, A.; Powar, S.; J. Mozer, A.; Mena-Osteritz, E.; Cheng, Y.-B.; Bach, U.; Bäuerle, P. Synthesis and Characterization of Perylene–Bithiophene–Triphenylamine Triads: Studies on the Effect of Alkyl-Substitution in p-Type NiO Based Photocathodes. *Journal of Materials Chemistry* **2012**, 22 (15), 7366–7379. <https://doi.org/10.1039/C2JM16847B>.
- (31) Bai, Y.; Zhang, J.; Zhou, D.; Wang, Y.; Zhang, M.; Wang, P. Engineering Organic Sensitizers for Iodine-Free Dye-Sensitized Solar Cells: Red-Shifted Current Response Concomitant with



- Attenuated Charge Recombination. *J. Am. Chem. Soc.* **2011**, *133* (30), 11442–11445. <https://doi.org/10.1021/ja203708k>.
- (32) Gao, P.; Kim, Y. J.; Yum, J.-H.; Holcombe, T. W.; Nazeeruddin, M. K.; Grätzel, M. Facile Synthesis of a Bulky BTPA Donor Group Suitable for Cobalt Electrolyte Based Dye Sensitized Solar Cells. *J. Mater. Chem. A* **2013**, *1* (18), 5535–5544. <https://doi.org/10.1039/C3TA10632B>.
- (33) Mathew, S.; Yella, A.; Gao, P.; Humphry-Baker, R.; Curchod, B. F. E.; Ashari-Astani, N.; Tavernelli, I.; Rothlisberger, U.; Nazeeruddin, M. K.; Grätzel, M. Dye-Sensitized Solar Cells with 13% Efficiency Achieved through the Molecular Engineering of Porphyrin Sensitizers. *Nature Chem* **2014**, *6* (3), 242–247. <https://doi.org/10.1038/nchem.1861>.
- (34) Choi, H.; Baik, C.; Kang, S. O.; Ko, J.; Kang, M.-S.; Nazeeruddin, M. K.; Grätzel, M. Highly Efficient and Thermally Stable Organic Sensitizers for Solvent-Free Dye-Sensitized Solar Cells. *Angewandte Chemie International Edition* **2008**, *47* (2), 327–330. <https://doi.org/10.1002/anie.200703852>.
- (35) Tang, Y.; Wang, Y.; Li, X.; Ågren, H.; Zhu, W.-H.; Xie, Y. Porphyrins Containing a Triphenylamine Donor and up to Eight Alkoxy Chains for Dye-Sensitized Solar Cells: A High Efficiency of 10.9%. *ACS Appl. Mater. Interfaces* **2015**, *7* (50), 27976–27985. <https://doi.org/10.1021/acsami.5b10624>.
- (36) Grimme, S.; Bannwarth, C.; Shushkov, P. A Robust and Accurate Tight-Binding Quantum Chemical Method for Structures, Vibrational Frequencies, and Noncovalent Interactions of Large Molecular Systems Parametrized for All Spd-Block Elements (Z = 1–86). *J. Chem. Theory Comput.* **2017**, *13* (5), 1989–2009. <https://doi.org/10.1021/acs.jctc.7b00118>.
- (37) Rego, L. G. C.; Batista, V. S. Quantum Dynamics Simulations of Interfacial Electron Transfer in Sensitized TiO<sub>2</sub> Semiconductors. *J. Am. Chem. Soc.* **2003**, *125* (26), 7989–7997. <https://doi.org/10.1021/ja0346330>.
- (38) da Silva, R.; Hoff, D. A.; Rego, L. G. C. Coupled Quantum-Classical Method for Long Range Charge Transfer: Relevance of the Nuclear Motion to the Quantum Electron Dynamics. *J. Phys.: Condens. Matter* **2015**, *27* (13), 134206. <https://doi.org/10.1088/0953-8984/27/13/134206>.
- (39) Dohm, S.; Bursch, M.; Hansen, A.; Grimme, S. Semiautomated Transition State Localization for Organometallic Complexes with Semiempirical Quantum Chemical Methods. *J. Chem. Theory Comput.* **2020**, *16* (3), 2002–2012. <https://doi.org/10.1021/acs.jctc.9b01266>.
- (40) Bursch, M.; Hansen, A.; Grimme, S. Fast and Reasonable Geometry Optimization of Lanthanoid Complexes with an Extended Tight Binding Quantum Chemical Method. *Inorg. Chem.* **2017**, *56* (20), 12485–12491. <https://doi.org/10.1021/acs.inorgchem.7b01950>.
- (41) Bursch, M.; Neugebauer, H.; Grimme, S. Structure Optimisation of Large Transition-Metal Complexes with Extended Tight-Binding Methods. *Angew. Chem., Int. Ed.* **2019**, *58* (32), 11078–11087. <https://doi.org/10.1002/anie.201904021>.
- (42) Bannwarth, C.; Caldeweyher, E.; Ehlert, S.; Hansen, A.; Pracht, P.; Seibert, J.; Spicher, S.; Grimme, S. Extended Tight-Binding Quantum Chemistry Methods. *WIREs Computational Molecular Science* n/a (n/a), e01493. <https://doi.org/10.1002/wcms.1493>.
- (43) Menzel, J. P.; Kloppenburg, M.; Belić, J.; Groot, H. J. M. de; Visscher, L.; Buda, F. Efficient Workflow for the Investigation of the Catalytic Cycle of Water Oxidation Catalysts: Combining GFN-XTB and Density Functional Theory. *Journal of Computational Chemistry* **2021**, *42* (26), 1885–1894. <https://doi.org/10.1002/jcc.26721>.
- (44) Bakker, T. M. A.; Menzel, J. P.; Vreugdenhil, B.; Bouwens, T.; Mathew, S.; Buda, F.; Reek, J. N. H. Increased Photocurrent by Improving the Donating Properties of the Anchoring Group in P-Type Dye Sensitized Solar Cells. *to be submitted*.
- (45) Hoff, D. A.; da Silva, R.; Rego, L. G. C. Coupled Electron–Hole Quantum Dynamics on D– $\pi$ –A Dye-Sensitized TiO<sub>2</sub> Semiconductors. *J. Phys. Chem. C* **2012**, *116* (40), 21169–21178. <https://doi.org/10.1021/jp303647x>.
- (46) Velde, G. te; Bickelhaupt, F. M.; Baerends, E. J.; Fonseca Guerra, C.; van Gisbergen, S. J. A.; Snijders, J. G.; Ziegler, T. Chemistry with ADF. *J. Comput. Chem.* **2001**, *22* (9), 931–967.



- (47) ADF 2020.3, SCM, Theoretical Chemistry, Vrije Universiteit, Amsterdam, The Netherlands, <http://www.scm.com>.
- (48) AMS2020.3, SCM, Theoretical Chemistry, Vrije Universiteit, Amsterdam, The Netherlands, <http://www.scm.com>.
- (49) AMS DFTB 2020.3, SCM, Theoretical Chemistry, Vrije Universiteit, Amsterdam, The Netherlands, <http://www.scm.com>.
- (50) Berendsen, H. J. C.; Postma, J. P. M.; van Gunsteren, W. F.; DiNola, A.; Haak, J. R. Molecular Dynamics with Coupling to an External Bath. *J. Chem. Phys.* **1984**, *81* (8), 3684–3690. <https://doi.org/10.1063/1.448118>.
- (51) Becke, A. D. A New Mixing of Hartree–Fock and Local Density-functional Theories. *J. Chem. Phys.* **1993**, *98* (2), 1372–1377. <https://doi.org/10.1063/1.464304>.
- (52) Lee, C.; Yang, W.; Parr, R. G. Development of the Colle-Salvetti Correlation-Energy Formula into a Functional of the Electron Density. *Phys. Rev. B* **1988**, *37* (2), 785–789.
- (53) Van Lenthe, E.; Baerends, E. J. Optimized Slater-Type Basis Sets for the Elements 1–118. *J. Comput. Chem.* **2003**, *24*, 1142–1156.
- (54) Grimme, S.; Ehrlich, S.; Goerigk, L. Effect of the Damping Function in Dispersion Corrected Density Functional Theory. *J. Comput. Chem.* **2011**, *32* (7), 1456–1465. <https://doi.org/10.1002/jcc.21759>.
- (55) Sakai, N.; Mareda, J.; Vauthey, E.; Matile, S. Core-Substituted Naphthalenediimides. *Chem. Commun.* **2010**, *46* (24), 4225–4237.
- (56) Ooyama, Y.; Yamaji, K.; Ohshita, J. Photovoltaic Performances of Type-II Dye-Sensitized Solar Cells Based on Catechol Dye Sensitizers: Retardation of Back-Electron Transfer by PET (Photo-Induced Electron Transfer). *Mater. Chem. Front.* **2017**, *1* (11), 2243–2255. <https://doi.org/10.1039/C7QM00211D>.
- (57) Monti, A.; Negre, C. F. A.; Batista, V. S.; Rego, L. G. C.; de Groot, H. J. M.; Buda, F. Crucial Role of Nuclear Dynamics for Electron Injection in a Dye–Semiconductor Complex. *J. Phys. Chem. Lett.* **2015**, *6* (12), 2393–2398.
- (58) Yanai, T.; Tew, D. P.; Handy, N. C. A New Hybrid Exchange–Correlation Functional Using the Coulomb-Attenuating Method (CAM-B3LYP). *Chem. Phys. Lett.* **2004**, *393* (1), 51–57. <https://doi.org/10.1016/j.cplett.2004.06.011>.
- (59) Akinaga, Y.; Ten-no, S. Range-Separation by the Yukawa Potential in Long-Range Corrected Density Functional Theory with Gaussian-Type Basis Functions. *Chem. Phys. Lett.* **2008**, *462* (4), 348–351. <https://doi.org/10.1016/j.cplett.2008.07.103>.
- (60) Seth, M.; Ziegler, T. Range-Separated Exchange Functionals with Slater-Type Functions. *J. Chem. Theory Comput.* **2012**, *8* (3), 901–907. <https://doi.org/10.1021/ct300006h>.



## 6.A Appendix

### 6A.1 Geometry Comparison between GFN-xTB and B3LYP

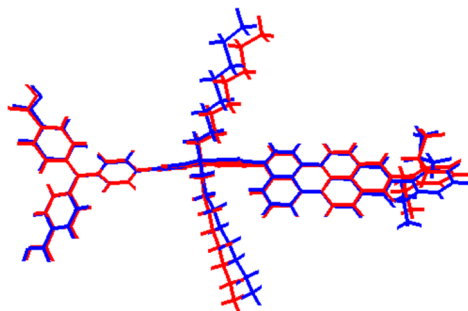


**Figure 6A.1** Comparison of the GFN-xTB optimized geometry (red) with the B3LYP optimized geometry (blue) for the TPA-FLU-PMI dye.

### 6A.2 Optimization of Extended Hückel Parameters

**Table 6A.1:** Experimental redox potentials vs. NHE and vacuum from CV measurements, onset of absorption peak in UV-VIS and estimated reduction potential for the four fragment molecules and two push-pull dyes

Molecule	Oxidation Potential [V] (CV)	Reduction Potential [V] (CV)	UV-VIS absorption onset [nm]/(eV)	Red. Pot. estimate (Ox. Pot - UV-VIS onset) [V]
TPA	1.20	-	380 nm (3.26 eV)	-2.06
EDG-TPA	0.90	-	350 nm (3.54 eV)	-2.64
Fluorene	1.70	-	315 nm (3.94 eV)	-2.55
PMI	1.35	-1.02	-	-
TPA-FLU-PMI	1.05	-1.00	-	-
EDG-TPA-FLU-PMI	0.85	-1.00	-	-

Since the relative alignment of these energies is important, first the PMI was optimized to provide a realistic estimate of the HOMO-LUMO gap. The energies obtained with these optimized parameters (HOMO: -11.80 eV, LUMO: -9.43 eV) had a total shift of 6.01 eV in comparison to the targeted orbital energies, so all target energies were shifted by this 6.01 eV. All other molecules were then optimized to give the same energetic alignment as the experimental values using this 6.01 eV shift. The TPA-FLU-PMI and EDG-TPA-FLU-PMI dyes were not reoptimized, but the parameters for the molecular fragments were used. The agreement with the target values derived from experiment were very good with deviations in the range 0.02 – 0.05 eV.

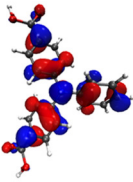
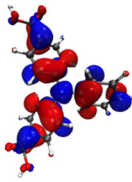
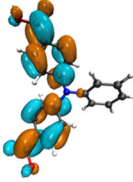
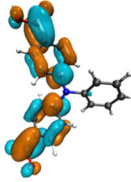
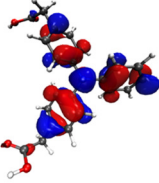
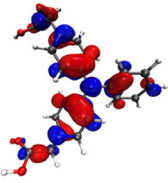
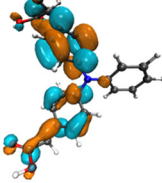
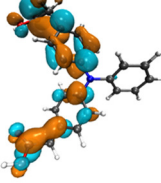
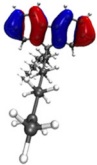
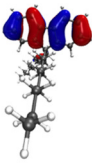
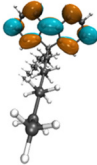
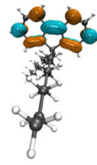
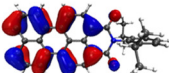
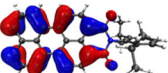
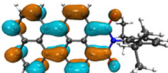
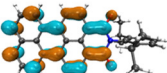


## CHAPTER 6

**Table 6A.2:** HOMO and LUMO energies for TPA, EDG-TPA, Fluorene, PMI, TPA-FLU-PMI and EDG-TPA-FLU-PMI obtained with standard Hückel parameters, target values generated with a linear shift of -6.01 eV and obtained with the optimized Hückel parameters.

Molecule	Standard Hückel Parameters [eV]		Target values [eV]		Optimized Hückel parameters [eV]	
	HOMO	LUMO	HOMO	LUMO	HOMO	LUMO
TPA	-11.56	-9.45	-11.65	-8.39	-11.64	-8.38
EDG-TPA	-11.36	-8.51	-11.35	-7.81	-11.35	-7.80
Fluorene	-12.11	-8.89	-12.15	-8.26	-12.15	-8.25
PMI	-11.74	-10.33	-11.80	-9.43	-11.80	-9.42
TPA-FLU-PMI	-11.47	-10.30	-11.50	-9.45	-11.47	-9.40
EDG-TPA-FLU-PMI	-11.30	-10.30	-11.30	-9.45	-11.32	-9.40

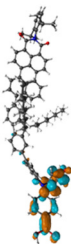
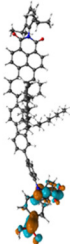
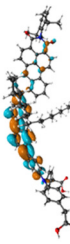
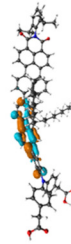
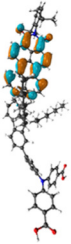
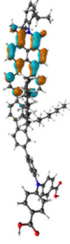
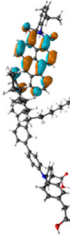
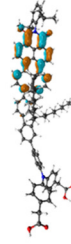
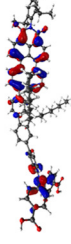
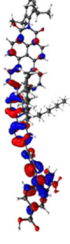
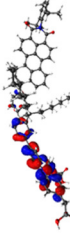
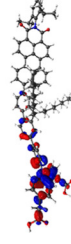
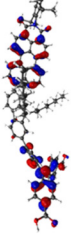
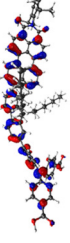
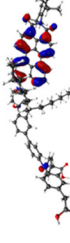
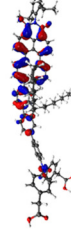
**Table 6A.3:** Spatial distribution of HOMO and LUMO for the four fragment molecules, using B3LYP and the Extended Hückel method with optimized parameters.

Molecule /Method	HOMO		LUMO	
	B3LYP	Extended Hückel	B3LYP	Extended Hückel
TPA				
EDG-TPA				
Fluorene				
PMI				



## In silico Optimization of Charge Separating Dyes

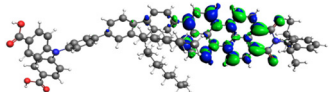
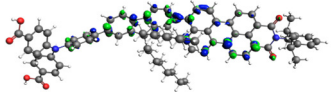
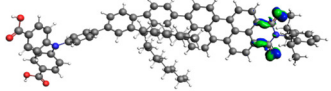
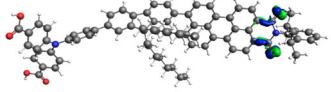
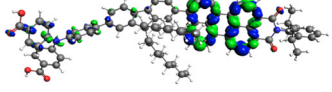
**Table 6A.4:** Spatial distribution of HOMO-1, HOMO, LUMO and LUMO+1 for the TPA-FLU-PMI and EDG-TPA-FLU-PMI dyes, using B3LYP and Extended Hückel method with optimized parameters. Note the different LUMO+1 localization between the dyes.

Molecule	TPA-FLU-PMI		EDG-TPA-FLU-PMI	
Method	B3LYP	Extended Hückel	B3LYP	Extended Hückel
LUMO+1				
LUMO				
HOMO				
HOMO-1				

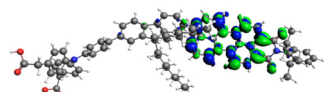
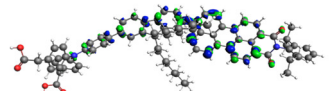
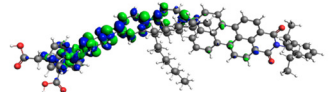
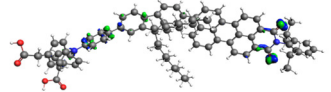
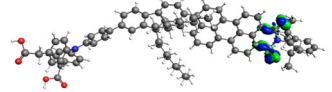


## 6A.3 Relevant Excitations

**Table 6A.5:** TDDFT transitions for the COOH-TPA-FLU-PMI dye, including excitation energy, oscillator strength and transition densities.

Transition Nr.	Excitation energy [nm]	Oscillator strength	Transition density
1	466 nm	1.117	
2	352 nm	0.109	
3	330 nm	0.000	
4	329 nm	0.001	
5	327 nm	0.1030	

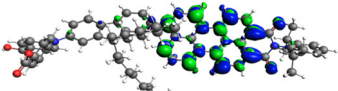
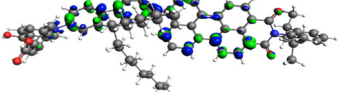
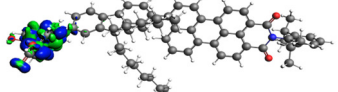
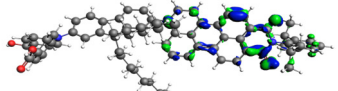
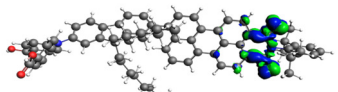
**Table 6A.6:** TDDFT transitions for the EDG-TPA-FLU-PMI dye, including excitation energy, oscillator strength and transition densities.

Transition Nr.	Excitation energy [nm]	Oscillator strength	Transition density
1	464 nm	1.082	
2	379 nm	0.016	
3	331 nm	1.248	
4	329 nm	0.019	
5	328 nm	0.000	

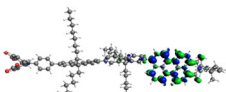
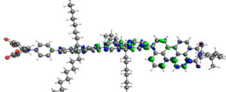
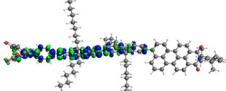
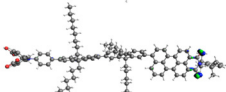
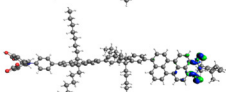


## In silico Optimization of Charge Separating Dyes

**Table 6A.7:** TDDFT transitions for the DPA-FLU-PMI dye, including excitation energy, oscillator strength and transition densities.

Transition Nr.	Excitation energy [nm]	Oscillator strength	Transition density
1	466 nm	1.090	
2	365 nm	0.045	
3	333 nm	0.436	
4	330 nm	0.000	
5	330 nm	0.000	

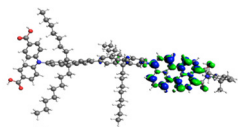
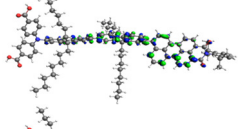
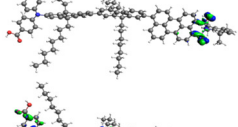
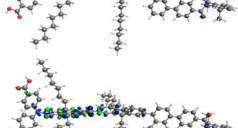
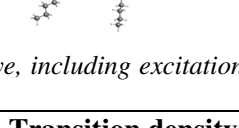
**Table 6A.8:** TDDFT transitions for the TPA-2FLU-PMI dye, including excitation energy, oscillator strength and transition densities.

Transition Nr.	Excitation energy [nm]	Oscillator strength	Transition density
1	470 nm	1.280	
2	359 nm	0.215	
3	332 nm	2.139	
4	330 nm	0.007	
5	329 nm	0.006	

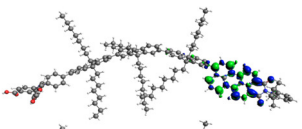
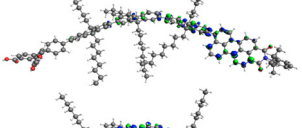
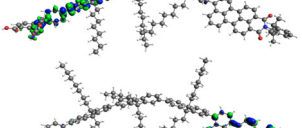
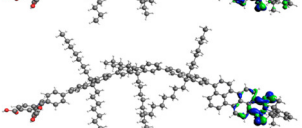



## CHAPTER 6

**Table 6A.9:** TDDFT transitions for the DPA-2FLU-PMI dye, including excitation energy, oscillator strength and transition densities.

Transition Nr.	Excitation energy [nm]	Oscillator strength	Transition density
1	470 nm	1.254	
2	356 nm	0.213	
3	331 nm	0.006	
4	330 nm	1.081	
5	329 nm	0.281	

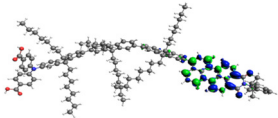
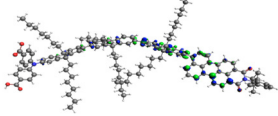
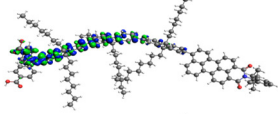
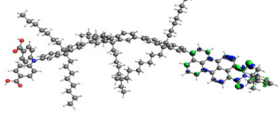
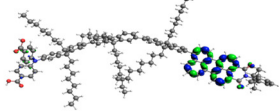
**Table 6A.10:** TDDFT transitions for the TPA-3FLU-PMI dye, including excitation energy, oscillator strength and transition densities.

Transition Nr.	Excitation energy [nm]	Oscillator strength	Transition density
1	469 nm	1.228	
2	356 nm	0.215	
3	335 nm	2.682	
4	330 nm	0.000	
5	329 nm	0.001	

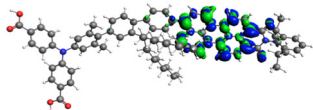
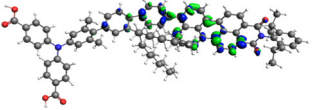
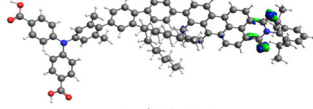
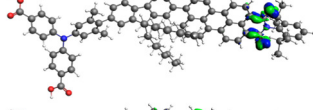
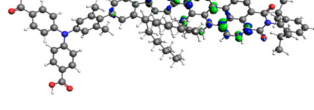


## In silico Optimization of Charge Separating Dyes

**Table 6A.11:** TDDFT transitions for the DPA-3FLU-PMI dye, including excitation energy, oscillator strength and transition densities.

Transition Nr.	Excitation energy [nm]	Oscillator strength	Transition density
1	468 nm	1.213	
2	354 nm	0.202	
3	336 nm	1.858	
4	330 nm	0.000	
5	327 nm	0.031	

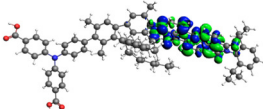
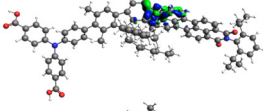
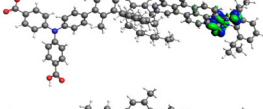
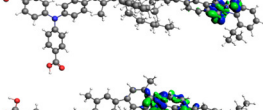

**Table 6A.12:** TDDFT transitions for the TPAMe-FLU-PMI dye, including excitation energy, oscillator strength and transition densities.

Transition Nr.	Excitation energy [nm]	Oscillator strength	Transition density
1	465 nm	1.044	
2	337 nm	0.036	
3	330 nm	0.001	
4	330 nm	0.000	
5	324 nm	0.001	

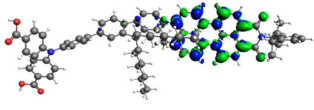
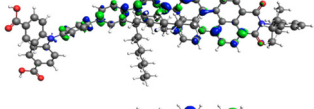
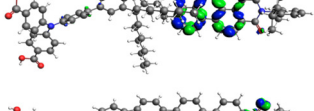
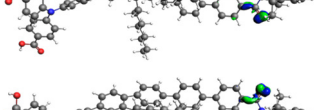



## CHAPTER 6

**Table 6A.13:** TDDFT transitions for the TPA-FLUMe-PMI dye, including excitation energy, oscillator strength and transition densities.

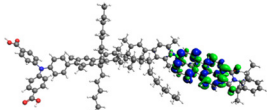
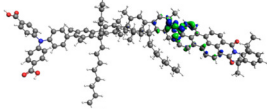
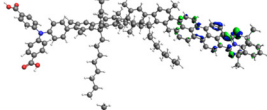
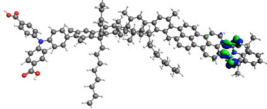
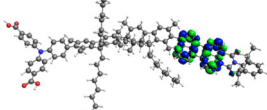
Transition Nr.	Excitation energy [nm]	Oscillator strength	Transition density
1	459 nm	0.914	
2	365 nm	0.000	
3	328 nm	0.000	
4	328 nm	0.000	
5	313 nm	0.000	

**Table 6A.14:** TDDFT transitions for the TPA-FLU-PMIME dye, including excitation energy, oscillator strength and transition densities.

Transition Nr.	Excitation energy [nm]	Oscillator strength	Transition density
1	477 nm	1.165	
2	353 nm	0.194	
3	330 nm	0.022	
4	329 nm	0.004	
5	328 nm	0.001	



**Table 6A.15:** TDDFT transitions for the TPA-2FLUMe-PMI dye, including excitation energy, oscillator strength and transition densities.

Transition Nr.	Excitation energy [nm]	Oscillator strength	Transition density
1	460 nm	1.038	
2	369 nm	0.000	
3	329 nm	0.000	
4	328 nm	0.002	
5	327 nm	0.001	

#### 6A.4 Electron and hole migration in the TPA-FLU-PMI dye

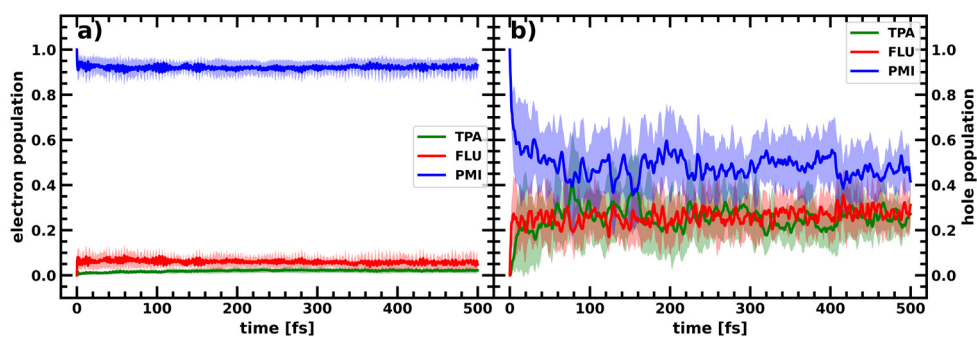


**Figure 6A.2.** Electron (a) and hole (b) populations over time on the fragments TPA (green), FLU (red) and PMI (blue) of the TPA-FLU-PMI dye. Only the hole shows significant population transfer.



## 6A.5 Average charges on fragments of all investigated dyes

**Table 6A.16:** Mean charge on the fragments of all investigated dyes, averaged over 10 CTDs and the last 200fs. The TPA-FLU-PMI simulations were performed twice for comparison with EDG-TPA-FLU-PMI and the other molecules, with high quantitative agreement.

Dye	Charge on Donor	Charge on FLU	Charge on PMI
TPA-FLU-PMI	+0.23/+0.24	+0.20/+0.20	-0.43/-0.44
EDG-TPA-FLU-PMI	+0.30	+0.23	-0.53
DPA-FLU-PMI	+0.20	+0.26	-0.46
TPA-2FLU-PMI	+0.21	+0.33	-0.54
DPA-2FLU-PMI	+0.16	+0.37	-0.53
TPA-3FLU-PMI	+0.13	+0.41	-0.54
DPA-3FLU-PMI	+0.13	+0.43	-0.56
TPAMe-FLU-PMI	+0.28	+0.21	-0.49
TPA-FLUMe-PMI	+0.26	+0.29	-0.55
TPA-FLU-PMIMe	+0.22	+0.22	-0.43
TPA-2FLUMe-PMI	+0.19	+0.47	-0.66

## 6A.6 Charge accumulation on the Donor: TPA-2FLU-PMI vs DPA-2FLU-PMI

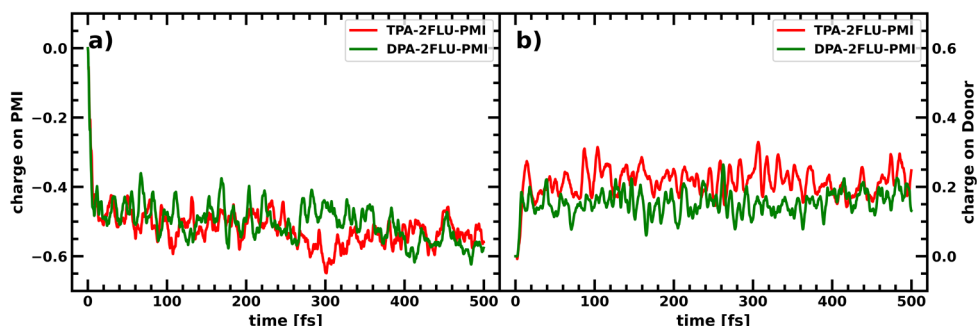


**Figure 6.A3.** a) Average charge accumulation averaged over 10 CTDs on the PMI in the TPA-2FLU-PMI (red) and DPA-2FLU-PMI (green) dyes upon photoexcitation of the PMI. b) Average charge accumulation averaged over 10 CTDs on the donor (TPA/DPA) in the TPA-2FLU-PMI (red) and DPA-2FLU-PMI (green) dyes upon photoexcitation of the PMI.



### 6A.7 UV-VIS spectra of DPA-XFLU-PMI dyes

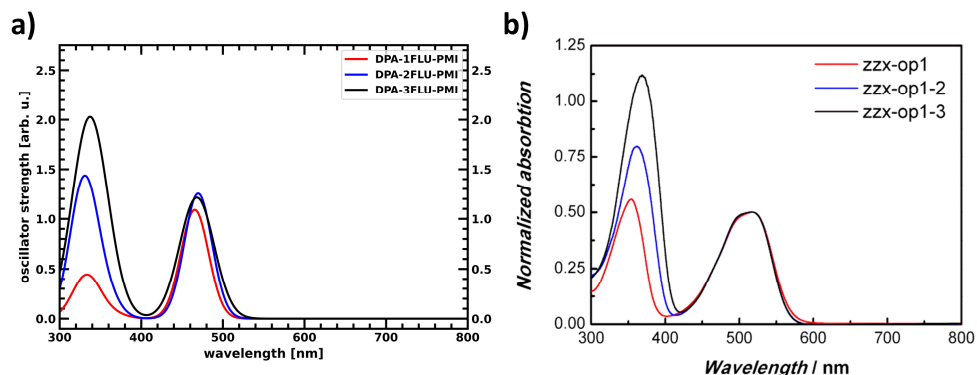


**Figure 6.A4.** UV-VIS spectra of the charge separating dyes with DPA-xFLU-PMI structure. Note the increasing oscillator strength/absorption of the lower energetic peak with increasing number of fluorenes. **a)** obtained by TDDFT calculations above (tables 6A.7, 6A.9 and 6A.11), **b)** experimental UV-VIS spectra with zzx-op1 corresponding to DPA-1FLU-PMI, zzx-op1-2 corresponding to DPA-2FLU-PMI and zzx-op1-3 corresponding to DPA-3FLU-PMI. Adapted with permission from: Liu, Z.; Li, W.; Topa, S.; Xu, X.; Zeng, X.; Zhao, Z.; Wang, M.; Chen, W.; Wang, F.; Cheng, Y.-B.; He, H. Fine Tuning of Fluorene-Based Dye Structures for High-Efficiency p-Type Dye-Sensitized Solar Cells. *ACS Appl. Mater. Interfaces* 2014, 6 (13), 10614–10622 (reference [18]). Copyright 2014 American Chemical Society.



